Spatio-temporal characterization of intense few-cycle 2 µm pulses

Dane R. Austin, Tobias Witting, Sébastien J. Weber, Peng Ye, Thomas Siegel, Paloma Matía-Hernando, Allan S. Johnson, John W.G. Tisch, and Jonathan P. Marangos

Blackett Laboratory, Imperial College, London SW7 2AZ,UK
Corresponding author: d.austin@imperial.ac.uk

Abstract: We present a variant of spatially encoded spectral shearing interferometry for measuring two-dimensional spatio-temporal slices of few-cycle pulses centered around 2 µm. We demonstrate experimentally that the device accurately retrieves the pulse-front tilt caused by angular dispersion of two-cycle pulses. We then use the technique to characterize 500–650 µJ pulses from a hollow fiber pulse compressor, with durations as short as 7.1 fs (1.3 optical cycles).

© 2016 Optical Society of America

OCIS codes: 320.0320, 320.7100, 320.7160, 320.5520

References and links

1. E. Goulielmakis, M. Schultze, M. Hofstetter, V. S. Yakovlev, J. Gagnon, M. Uiberacker, A. L. Aquila, E. M. Gullikson, D. T. Attwood, R. Kienberger, F. Krausz, and U. Kleineberg, "Single-cycle nonlinear optics," Science **320**, 1614–1617 (2008).
2. M. Uiberacker, T. Uphues, M. Schultze, A. J. Verhoef, V. Yakovlev, M. F. Kling, J. Rauschenberger, N. M. Kabachnik, H. Schröder, M. Lezius, K. L. Kompa, H.-G. Muller, M. J. J. Vrakking, S. Hendel, U. Kleineberg, U. Heinzmann, M. Drescher, and F. Krausz, "Attosecond real-time observation of electron tunnelling in atoms," Nature **446**, 627–632 (2007).
3. E. Goulielmakis, Z.-H. Loh, A. Wirth, R. Santra, N. Rohringer, V. S. Yakovlev, S. Zherebtsov, T. Pfeifer, A. M. Azzeer, M. F. Kling, S. R. Leone, and F. Krausz, "Real-time observation of valence electron motion," Nature **466**, 739–743 (2010).
4. M. Schultze, E. M. Bothschafter, A. Sommer, S. Holzner, W. Schweinberger, M. Fiess, M. Hofstetter, R. Kienberger, V. Apalkov, V. S. Yakovlev, M. I. Stockman, and F. Krausz, "Controlling dielectrics with the electric field of light," Nature **493**, 75–78 (2013).
5. M. Nisoli, S. D. Silvestri, and O. Svelto, "Generation of high energy 10 fs pulses by a new pulse compression technique," Appl. Phys. Lett. **68**, 2793–2795 (1996).
6. T. Witting, F. Frank, C. A. Arrell, W. A. Okell, J. P. Marangos, and J. W. G. Tisch, "Characterization of high-intensity sub-4-fs laser pulses using spatially encoded spectral shearing interferometry," Opt. Lett. **36**, 1680–1682 (2011).
7. A. L. Cavalieri, E. Goulielmakis, B. Horvath, W. Helml, M. Schultze, M. FieSS, V. Pervak, L. Veisz, V. S. Yakovlev, M. Uiberacker, A. Apolonski, F. Krausz, and R. Kienberger, "Intense 1.5-cycle near infrared laser waveforms and their use for the generation of ultra-broadband soft-x-ray harmonic continua," New J. Phys. **9**, 242 (2007).
8. F. Böhle, M. Kretschmar, A. Jullien, M. Kovacs, M. Miranda, R. Romero, H. Crespo, U. Morgner, P. Simon, R. Lopez-Martens, and T. Nagy, "Compression of CEP-stable multi-mJ laser pulses down to 4 fs in long hollow fibers," Laser Phys. Lett. **11**, 095401 (2014).
9. P. Colosimo, G. Doumy, C. I. Blaga, J. Wheeler, C. Hauri, F. Catoire, J. Tate, R. Chirla, A. M. March, G. G. Paulus, H. G. Muller, P. Agostini, and L. F. DiMauro, "Scaling strong-field interactions towards the classical limit," Nat. Phys. **4**, 386–389 (2008).
10. T. Popmintchev, M.-C. Chen, O. Cohen, M. E. Grisham, J. J. Rocca, M. M. Murnane, and H. C. Kapteyn, "Extended phase matching of high harmonics driven by mid-infrared light," Opt. Lett. **33**, 2128–2130 (2008).
11. C. Vozzi, R. Torres, M. Negro, L. Brugnera, T. Siegel, C. Altucci, R. Velotta, F. Frassetto, L. Poletto, P. Villoresi, S. De Silvestri, S. Stagira, and J. P. Marangos, "High harmonic generation spectroscopy of hydrocarbons," Appl. Phys. Lett. **97**, 241103 (2010).
12. Y. Deng, A. Schwarz, H. Fattahi, M. Ueffing, X. Gu, M. Ossiander, T. Metzger, V. Pervak, H. Ishizuki, T. Taira, T. Kobayashi, G. Marcus, F. Krausz, R. Kienberger, and N. Karpowicz, "Carrier-envelope-phase-stable, 1.2 mJ, 1.5 cycle laser pulses at 2.1 µm," Opt. Lett. **37**, 4973–4975 (2012).
13. C. P. Hauri, R. B. Lopez-Martens, C. I. Blaga, K. D. Schultz, J. Cryan, R. Chirla, P. Colosimo, G. Doumy, A. M. March, C. Roedig, E. Sistrunk, J. Tate, J. Wheeler, L. F. DiMauro, and E. P. Power, "Intense self-compressed and self-phase-stabilized few-cycle pulses at 2 µm from an optical filament," Opt. Lett. **32**, 868–870 (2007).
14. B. E. Schmidt, P. Béjot, M. Giguère, A. D. Shiner, C. Trallero-Herrero, Éric Bisson, J. Kasparian, J.-P. Wolf, D. M. Villeneuve, J.-C. Kieffer, P. B. Corkum, and F. Légaré, "Compression of 1.8 µm laser pulses to sub two optical cycles

with bulk material," Appl. Phys. Lett. **96**, 121109 (2010).
15. B. E. Schmidt, A. D. Shiner, P. Lassonde, J.-C. Kieffer, P. B. Corkum, D. M. Villeneuve, and F. Légaré, "CEP stable 1.6 cycle laser pulses at 1.8 µm," Opt. Express **19**, 6858–6864 (2011).
16. A. Baltuška, T. Fuji, and T. Kobayashi, "Controlling the carrier-envelope phase of ultrashort light pulses with optical parametric amplifiers," Phys. Rev. Lett. **88**, 133901 (2002).
17. C. Li, D. Wang, L. Song, J. Liu, P. Liu, C. Xu, Y. Leng, R. Li, and Z. Xu, "Generation of carrier-envelope phase stabilized intense 1.5 cycle pulses at 1.75 µm," Opt. Express **19**, 6783–6789 (2011).
18. R. Trebino, K. W. DeLong, D. N. Fittinghoff, J. N. Sweetser, M. A. Krumbügel, B. A. Richman, and D. J. Kane, "Measuring ultrashort laser pulses in the time-frequency domain using frequency-resolved optical gating," Rev. Sci. Instrum. **68**, 3277–3295 (1997).
19. S. Baker, J. S. Robinson, C. A. Haworth, H. Teng, R. A. Smith, C. C. Chirilă, M. Lein, J. W. G. Tisch, and J. P. Marangos, "Probing proton dynamics in molecules on an attosecond time scale," Science **312**, 424–427 (2006).
20. I. V. Pogorelsky, I. Ben-Zvi, J. Skaritka, M. Babzien, M. N. Polyanskiy, Z. Najmudin, N. Dover, and W. Lu, "New opportunities for strong-field LPI research in the mid-IR," Proc. SPIE **9509** (2015).
21. P. Gabolde and R. Trebino, "Self-referenced measurement of the complete electric field of ultrashort pulses," Opt. Express **12**, 4423–4429 (2004).
22. B. Alonso, M. Miranda, I. J. Sola, and H. Crespo, "Spatiotemporal characterization of few-cycle laser pulses," Opt. Express **20**, 17880–17893 (2012).
23. C. Dorrer, E. Kosik, and I. Walmsley, "Spatio-temporal characterization of the electric field of ultrashort optical pulses using two-dimensional shearing interferometry," Appl. Phys. B: Lasers Opt. **74**, 209–217 (2002).
24. E. Rubino, D. Faccio, L. Tartara, P. K. Bates, O. Chalus, M. Clerici, F. Bonaretti, J. Biegert, and P. D. Trapani, "Spatiotemporal amplitude and phase retrieval of space-time coupled ultrashort pulses using the Shackled-FROG technique," Opt. Lett. **34**, 3854–3856 (2009).
25. G. Fan, T. Balčiūnas, C. Fourcade-Dutin, S. Haessler, A. A. Voronin, A. M. Zheltikov, F. Gérôme, F. Benabid, A. Baltuška, and T. Witting, "X-sea-f-spider characterization of over octave spanning pulses in the infrared range," Opt. Express **24**, 12713–12729 (2016).
26. T. Witting, D. R. Austin, T. Barillot, D. Greening, P. Matia-Hernando, D. Walke, J. P. Marangos, and J. W. G. Tisch, "Self-referenced characterization of space–time couplings in near-single-cycle laser pulses," Opt. Lett. **41**, 2382–2385 (2016).
27. Hebling and J., "Derivation of the pulse front tilt caused by angular dispersion," Opt. Quantum. Electron. **28**, 1759–1763 (1996).
28. Birge, JR, Kärtner, and FX, "Analysis and mitigation of systematic errors in spectral shearing interferometry of pulses approaching the single-cycle limit [Invited]," J. Opt. Soc. Am. B **25**, 25–6 (2008).
29. T. Witting, D. R. Austin, and I. A. Walmsley, "Improved ancilla preparation in spectral shearing interferometry for accurate ultrafast pulse characterization," Opt. Lett. **34**, 881–883 (2009).
30. T. Witting, S. J. Weber, J. W. G. Tisch, and J. P. Marangos, "Spatio-temporal characterization of mid-infrared laser pulses with spatially encoded spectral shearing interferometry," Opt. Express **20**, 27974–27980 (2012).
31. M. Hirasawa, N. Nakagawa, K. Yamamoto, R. Morita, H. Shigekawa, and M. Yamashita, "Sensitivity improvement of spectral phase interferometry for direct electric-field reconstruction for the characterization of low-intensity femtosecond pulses," Appl. Phys. B: Lasers Opt. **74**, s225–s229 (2002).
32. D. R. Austin, T. Witting, and I. A. Walmsley, "Broadband astigmatism-free Czerny-Turner imaging spectrometer using spherical mirrors," Appl. Opt. **48**, 3846–3853 (2009).
33. E. Kosik, A. Radunsky, I. A. Walmsley, and C. Dorrer, "Interferometric technique for measuring broadband ultrashort pulses at the sampling limit," Opt. Lett. **30**, 326–328 (2005).
34. A. S. Wyatt, A. Grün, P. K. Bates, O. Chalus, J. Biegert, and I. A. Walmsley, "Accuracy measurements and improvement for complete characterization of optical pulses from nonlinear processes via multiple spectral-shearing interferometry," Opt. Express **19**, 25355–25366 (2011).
35. D. R. Austin, T. Witting, and I. A. Walmsley, "High precision self-referenced phase retrieval of complex pulses with multiple-shearing spectral interferometry," J. Opt. Soc. Am. B **26**, 1818–1830 (2009).
36. A. S. Wyatt and I. A. Walmsley, "Analysis of space-time coupling in SEA-SPIDER measurements," in "European Conference on Lasers and Electro-Optics and the European Quantum Electronics Conference (CLEO/EQEC)," (2009).
37. A. S. Wyatt, I. A. Walmsley, G. Stibenz, and G. Steinmeyer, "Sub-10 fs pulse characterization using spatially encoded arrangement for spectral phase interferometry for direct electric field reconstruction," Opt. Lett. **31**, 1914–1916 (2006).
38. S. Akturk, X. Gu, E. Zeek, and R. Trebino, "Pulse-front tilt caused by spatial and temporal chirp," Opt. Express **12**, 4399–4410 (2004).
39. R. K. Nubling and J. A. Harrington, "Launch conditions and mode coupling in hollow-glass waveguides," Opt. Eng. **37**, 2454–2458 (1998).
40. W. A. Okell, T. Witting, D. Fabris, D. Austin, M. Bocoum, F. Frank, A. Ricci, A. Jullien, D. Walke, J. P. Marangos, R. Lopez-Martens, and J. W. G. Tisch, "Carrier-envelope phase stability of hollow fibers used for high-energy few-cycle pulse generation," Opt. Lett. **38**, 3918–3921 (2013).
41. B. Dromey, M. Zepf, M. Landreman, and S. M. Hooker, "Quasi-phasematching of harmonic generation via multimode

beating in waveguides," Opt. Express **15**, 7894–7900 (2007).
42. F. Tani, J. C. Travers, and P. S. Russell, "Multimode ultrafast nonlinear optics in optical waveguides: numerical modeling and experiments in kagomé photonic-crystal fiber," J. Opt. Soc. Am. B **31**, 311–320 (2014).
43. C.-J. Lai and F. X. Kärtner, "The influence of plasma defocusing in high harmonic generation," Opt. Express **19**, 22377–22387 (2011).

1. Introduction

Few-cycle laser pulses with stable electric field profiles and energies of 0.1–1 mJ are a primary tool of attoscience and strong-field physics, enabling the production of isolated attosecond pulses [1] for probing electronic motion on sub-femtosecond timescale [2–4]. Due to the wide availability of Ti:sapphire chirped-pulse amplifiers (CPAs), the first few-cycle systems [5] operated at a wavelength of 800 nm, which remains popular today [6–8]. However, using longer drive wavelengths has several advantages stemming from the λ^2 dependence of the ponderomotive potential of a continuum electron released in a strong field [9]. These include phase-matched high-order harmonic generation (HHG) above 150 eV [10] and extending the cutoff in HHG spectroscopy of samples with a low ionization potential [11].

There are several methods for producing few-cycle, mJ-level pulses at wavelengths longer than 800 nm. Optical parametric chirped pulse amplification (OPCPA) [12] offers a direct route, but its complexity motivates the compression of multi-cycle pulses available from simpler optical parametric amplification (OPA) systems. Filamentation in gases [13] offers great simplicity but is yet to achieve sub-two-cycle pulses and exhibits an intrinsic tradeoff between efficiency and beam quality due to its inherent spatio-temporal coupling. A proven technique is hollow-core fiber (HCF) compression of the idler pulses from an optical parametric amplifier pumped at 800 nm, first demonstrated by Schmidt et al. [14, 15]. Its advantages are that it is a mature technology for 800 nm pulses and can be transferred to new wavelengths straightforwardly, the required anomalous dispersion is simply and cheaply provided by bulk glass above ~1500 nm, and the difference frequency generation occurring in the OPA provides passive stability of the carrier-envelope phase (CEP) [16]. The current state-of-the-art for HCF compression is 8.4 fs pulses of energy 0.7 mJ at 1.75 μm [17].

With the development of long wavelength few-cycle sources comes the need for appropriate pulse characterization. The results to date [14, 15, 17] have used second harmonic generation frequency-resolved optical gating (SHG-FROG) [18], yielding a single one-dimensional temporal profile centered around 1800 nm. However, it is important to measure the spatio-temporal profiles; many applications, including HHG, are highly sensitive to the spatio-temporal profile of the driving field, and hollow core fibers, being only weakly guided, are susceptible to misalignment, bending, and other distortions which produce a sub-optimal spatial mode. Reproducible, well-controlled generation is particularly crucial for HHG spectroscopy [19] and attosecond pump-probe experiments. More generally, spatio-temporal characterization of few-cycle mid-infrared pulses will be beneficial for emerging applications such as filamentary propagation in air, material processing in dielectrics, and laser particle acceleration [20].

A common approach to spatio-temporal characterization is to combine temporal characterization of a point in the beam with spatially and spectrally resolved phase measurements using test-plus-reference interferometry [21, 22], lateral-shearing interferometry [23] or a Shack-Hartmann wavefront sensor [24]. Besides their additional complexity, these extensions can also be challenging for the broad bandwidths of few-cycle pulses, so for robustness and simplicity it is desirable to combine the roles of temporal and spatial characterization into one diagnostic. Spatially-encoded arrangement filter-based spectral phase interferometry for direct electric field reconstruction (SEA-F-SPIDER) is promising for this purpose. An adaption of the technique was recently shown to be capable of purely temporal characterization of pulses spanning 900–2200 nm [25]. Retrieval of certain spatio-temporal couplings at the focus of broadband visible pulses was

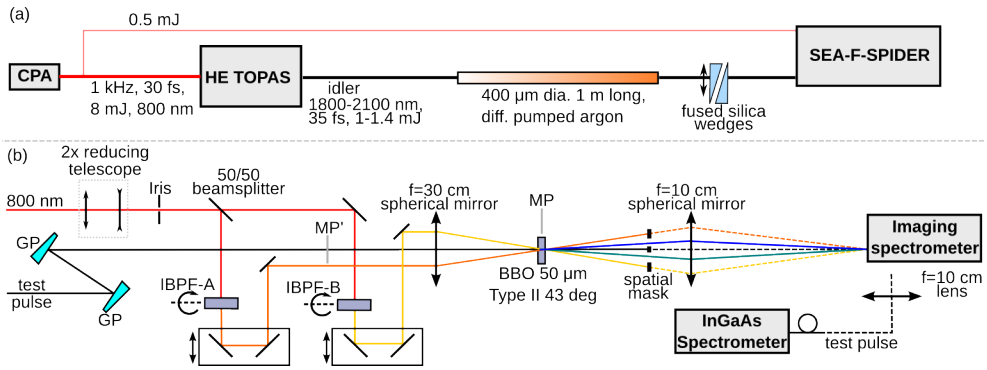

Fig. 1. Schematic of (a) entire setup for generation and characterization of few-cycle 2 µm pulses, and (b) SEA-F-SPIDER. Symbols are glass plate (GP), interferometric band-pass filter (IBPF), and measurement plane (MP). Dashed lines indicate beams used for auxiliary or calibration measurements.

also demonstrated [26]. Notably, the spatio-temporal couplings examined all involved spatial chirp, so that each point in the measurement plane contained a subset of the full bandwidth and was several times greater than the transform limit of the pulse. However, in the most basic spatio-temporal coupling, pulse-front tilt caused by angular dispersion [27], the full bandwidth is present at each point in the beam. Accurate diagnosis of this coupling in a few-cycle pulse therefore requires determination of the variation of the group delay across the beam to a precision of less than an optical cycle. Given the challenges of precision that arise with complex few-cycle pulses [28], as well as the complexity of moving to longer wavelengths, it therefore remains an open question whether SEA-F-SPIDER can retrieve general spatio-temporal couplings in the few-cycle mid-infrared regime.

Here, we use SEA-F-SPIDER [29] to perform the first spatio-temporal measurements of intense few-cycle pulses around 2 µm, with the pulses being produced by HCF compression. The measurements yield the pulse front across a one dimensional slice of the beam. We demonstrate the retrieval of pulse-front tilt caused by angular dispersion in few-cycle pulses, and observe the impact of various common misalignments of the input beam to the HCF. We also show that under optimum HCF coupling conditions, the reconstructed compressed pulses are spatially uniform and free of any pulse-front distortions, and demonstrate tuning of the pulse duration via the HCF gas pressure and tuning of the center wavelength.

2. Methods and preliminary measurements

2.1. Apparatus

Figure 1(a) summarizes the complete setup. A Ti:sapphire chirped pulse amplifier (CPA, Red Dragon, KM Labs) produces 8 mJ, 30 fs, 800 nm pulses at 1 kHz. These pump a commercial OPA (HE-TOPAS, Light Conversion Ltd), consisting of white light generation followed by three stages of amplification in beta barium borate (BBO). The signals from the first two stages are used as seeds for the subsequent stages. The idler from the third stage is selected by a dichroic mirror and then spectrally broadened and compressed using the scheme of Schmidt et al. [14, 15] as follows: the idler is focused into a 400 µm diameter, 1 m long HCF, differentially pumped with argon. Brewster mounted calcium fluoride windows of 1 mm thickness are used at both ends. The overall transmission efficiency is 45 ± 5%, depending on the input beam profile. After collimation, the spectrally broadened fiber output is compressed by the anomalous dispersion of a pair of fused silica wedges.

Spatio-temporal characterization is done with the SEA-F-SPIDER, shown in Fig. 1(b). The setup is based on ref. [30], but with several modifications for a high-fidelity spatio-temporal measurement of few-cycle pulses. Two glass reflections are used to attenuate the pulse energy to $\approx 1\,\mu$J. We use reflections rather than aperturing to ensure that the full pulse is measured, rather than the more spatially uniform central part. The beam is then focused into a 50 µm BBO crystal cut for Type II sum-frequency generation. The crystal defines the plane of measurement (labelled MP in Fig. 1(b)); the reconstructed pulse is therefore the far field of the conjugate plane (labelled MP'). To image the HCF exit face, MP' should lie in the rear focal plane of the HCF collimating mirror. In our setup MP' was ≈ 50 cm downstream due to layout constraints, but this propagation distance is negligible for the collimated beam.

To produce the quasi-monochromatic ancillae used for upconversion, we use a separate 800 nm beam [25, 31], picked off before the OPA. The beam is then split, with both portions passing interferometric band-pass filters (Semrock) with bandwidth 2.5 nm. The filters are mounted on motorized rotation stages, so that the transmitted wavelength can be varied from 808 nm (normal incidence) to 780 nm (15° incidence). The ancillae are combined with the test pulse with angle ± 2.5 deg to produce the upconverted replicas, which are selected with a spatial mask and reimaged onto the entrance slit of a home-built imaging spectrometer [32] by a $f = 10$ cm focal length spherical mirror. The ancillae can be also observed on the imaging spectrometer (dashed lines on Fig. 1(b)) for calibration of their frequency versus rotation stage angle. Note that the rotation axis of the band-pass filters lies in the interaction plane of the upconversion. In this way, the translation of the collimated ancilla beams caused by rotating their filters is perpendicular to the interaction plane. It therefore does not affect the crossing angle in the interaction plane, which determines the interferometric spatial carrier [33]. As will be discussed in section 2.2, this is important for accurate reconstruction of the pulse-front tilt. The spectral response of the spectrometer was calibrated using a tungsten lamp with known color temperature.

For temporal measurements of long-wavelength pulses, using a separate 800 nm beam for the ancillae has the advantages of decoupling the spectral intensity distribution of the test pulse from the measurement and bringing the upconverted signal into the spectral window of silicon detectors [25]. Additionally, for spatio-temporal measurements, the spatial quality of the ancillae is critical [34]. Using a separate beam decouples this from the test pulse, which may change often e.g. during alignment of the HCF. Note that the timing jitter between the ancillae and the test pulse is several femtoseconds. This is caused by air motion and pointing drift in the ≈ 10 m separated paths of the two beams, and was measured interferometrically. However, it has no effect on the reconstructed pulse because the ancillae are broadened to ~300 fs.

For each pulse reconstruction, we acquire a series of interferograms with different spectral shears, as well as a noninterferometric spatio-spectral intensity distribution, obtained by blocking of ancilla B. All adjustments are automated, and the typical exposure time of the imaging spectrometer camera is 50-200 ms; the total acquisition time is ≈ 1 second. We use multiple shear reconstructions [35] to improve the precision, which is particularly useful in here because the HCF output spectra are highly modulated. We use up to 4 shears, of size 15–60 mrad/fs (5–20 nm).

2.2. Analytic derivation of spatio-temporal reconstruction

Although SEA-SPIDER is generally taken as a spatio-temporal characterization technique, linear pulse-front tilt measurements were first demonstrated only recently [26]. It has been shown geometrically that SEA-SPIDER reconstructions contain an artificial pulse front tilt which can be corrected for [36], provided that the upconversion geometry is accurately calibrated [34]. However, a complete analytical treatment of spatio-temporal couplings in SEA-SPIDER is lacking from the literature. In this section we present such a treatment, which makes explicit any sources of error in the measurement.

We take the usual expression for the SEA-SPIDER signal [37], explicitly including the phase of the ancillae which cross with the test pulse at an angle θ in the crystal. The interferometric phase at observation frequency ω and position y with shear Ω is, up to an unknown but irrelevant constant

$$\Gamma(\omega+\omega_{\mathrm{A}}, y; \Omega) = \left[\phi_{\mathrm{T}}(\omega+\Omega, y) + \psi(\omega_{\mathrm{B}}, y) + \frac{\theta\omega_{\mathrm{B}} y}{c}\right] - \left[\phi_{\mathrm{T}}(\omega, y) + \psi(\omega_{\mathrm{A}}, y) - \frac{\theta\omega_{\mathrm{A}} y}{c}\right] \quad (1)$$

where ω_{A} is the frequency of ancilla A, $\omega_{\mathrm{B}} = \omega_{\mathrm{A}} - \Omega$ is the frequency of ancilla B, $\phi_{\mathrm{T}}(\omega, y)$ is the phase of the test pulse, and $\psi(\omega, y)$ the phase of the ancilla pulse. The calibration phase, taken with $\Omega = 0$, is

$$\Gamma(\omega+\omega_{\mathrm{A}}, y; 0) = \frac{2\theta\omega_{\mathrm{A}} y}{c}. \quad (2)$$

Here we have assumed that the crossing angle does not change between calibration and shear measurements. We satisfy this restriction in SEA-F-SPIDER by correct choice of the filter rotation axes, as described in section 2.1. The calibration phase can be subtracted to give

$$\Gamma_{\mathrm{c}}(\omega+\omega_{\mathrm{A}}, y; \Omega) = \Gamma(\omega+\omega_{\mathrm{A}}, y; \Omega) - \Gamma(\omega+\omega_{\mathrm{A}}, y; 0) \quad (3)$$

$$= \left[\psi(\omega_{\mathrm{B}}, y) - \psi(\omega_{\mathrm{A}}, y)\right] - \frac{\theta\Omega y}{c} + \Gamma_{\mathrm{i}}(\omega, y; \Omega). \quad (4)$$

The first term in (4) is the difference in the spatial phase of the ancillae at two frequencies separated by the shear. The error caused by this term decreases as the ancillae focii become more spatially uniform. Therefore, its impact can be estimated by adjusting the diameter of the iris through which the ancilla beam passes before focusing into the crystal (Fig. 1(a)). Reducing the diameter of the iris causes the ancillae focii to become larger and more uniform. If doing so causes no significant change in the reconstructed spatio-temporal profile, then it is unlikely that the spatial phase of the ancillae is affecting the result. We have verified this numerically.

The second term in (4) is the artificial pulse front tilt identified previously [36] and can be directly calculated and subtracted out by extracting θ from the calibration phase using (2). The final term in (4),

$$\Gamma_{\mathrm{i}}(\omega, y; \Omega) = \phi_{\mathrm{T}}(\omega+\Omega, y) - \phi_{\mathrm{T}}(\omega, y), \quad (5)$$

is the ideal spectral phase difference, correct up to a (y-independent) constant. Reconstructing the pulse using Γ_{i} returns the pulse front to first and higher orders, with the only ambiguities being the absolute group delay and a y-dependent integration phase corresponding to the wavefront, which is not returned by SEA-SPIDER.

Note that (1) implicitly uses the mean k-vector of the ancillae as the optical axis in the reconstruction of the test pulse. It is therefore essential to ensure that the test pulse propagates along this axis, which we accomplish by observing the overlap of the test pulse and the sum-frequency mixing of the ancillae in the far field after the crystal.

2.3. Verification measurements

In this section we present several experimental results that verify the claimed capabilities of the SEA-F-SPIDER.

To illustrate the sensitivity of SEA-F-SPIDER to pulse front distortions, we prepared an artificial pulse-front tilt by inserting 7.1 m of free space propagation between the compression wedges, as depicted in Fig. 2(a). The first wedge, acting as a prism, imparts an angular dispersion of 0.93 µrad/nm onto the pulse. This turns into a spatial chirp of 6.6 µm/nm as the pulse travels between the wedges. The angular dispersion is removed by the second wedge. Although this setup is qualitatively identical to the first half of a prism pulse compressor, the small (4°) apex angle of our prisms means that the negative chirp induced by propagation between the prisms is

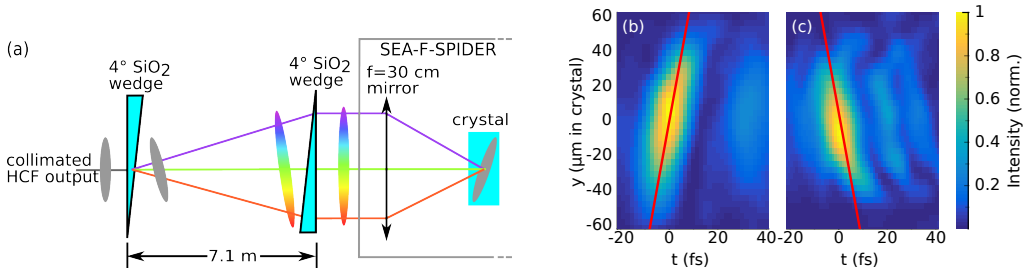

Fig. 2. (a)Setup for preparing near transform limited pulses with a tilted front in the focus. (b) Reconstructed spatio-temporal intensity (color scale) with theoretical pulse front tilt superimposed (red). (c) Same as (b), but with the wedge orientations reversed. The y-axis in (b) and (c) corresponds to the crystal plane.

not excessive, and additional negative chirp from material dispersion in the wedges is required to produce a transform-limited pulse. At the focus in the SEA-F-SPIDER crystal, the pulse has angular dispersion (but no spatial chirp), which produces [27] a pulse-front tilt of 40 mrad or 0.13 fs/μm. Figure 2(b) shows the retrieved spatio-temporal intensity. The predicted pulse front tilt is superimposed in red and shows good agreement. Using numerical cross-correlation to obtain the group delay as a function of position $\tau(y)$ and fitting a straight line, we obtain a pulse front tilt of 0.12 ± 0.01 fs/μm (mean and standard deviation of 10 consecutive measurements), close to the theoretical value. As a further verification we reversed the orientation of the wedges, which flips the sign of the pulse front tilt. The result is shown in Fig. 2(c), and also closely matches theory.

We note that this result goes beyond a recent demonstration of pulse-front tilt measurement using SEA-F-SPIDER [26], in which the PFT was generated by the combination of spatial chirp at the focus and temporal dispersion [38]. With this kind of PFT, the 1D temporal profile at any points in the focus has reduced bandwidth (due to the spatial chirp) and is temporally dispersed. Therefore, despite starting with an initially 1.3 cycle pulse (3.5 fs at 800 nm), the shortest profile for which a tilt was observed was 4.5 optical cycles (11.4 fs at 750 nm). Here, by contrast, we measure a PFT caused by pure angular dispersion in a pulse which is otherwise free of spatio-temporal distortions and nearly transform limited. As such, the 1D temporal profile has a duration of only 2.3 optical cycles (14.0 fs at 1800 nm). In terms of optical cycles, this is the shortest pulse for which PFT has been measured. In fact, as we show below, in its normal configuration our setup is capable of producing and measuring 1.3 cycle pulses. However, the air in the 7.1 m path between the wedges which we use for preparing the tilted focus introduces additional third-order spectral phase in the compressed pulses, preventing us from preparing an artificial PFT in the sub-2-cycle regime.

To ensure we had achieved accurate upconversion of the broadband test pulses, we compared the spectral intensity of the reconstructed pulse with that measured directly using a spectrometer with InGaAs detector (Ocean Optics NIRQuest-512) (Fig. 3(a)). The spectral range of the InGaAs spectrometer only extends up to 2100 nm, but within its range there is excellent agreement between the spectra. To obtain this level of agreement we found it necessary to carefully match the spatial regions of the beam used for the fundamental and SEA-F-SPIDER measurements. To robustly achieve this matching, we let the fundamental into the imaging spectrometer (black dashed line on Fig. 1(b)) and inserted a temporary pick-off mirror immediately after the entrance slit to send the beam into a 400 μm diameter core multimode optical fiber for delivery to the one-dimensional InGaAs spectrometer. The spectrum recorded by the InGaAs spectrometer can then be compared to the spatially integrated spectrum of the upconverted pulse recorded by the imaging spectrometer. The observed agreement is evidence that the upconverted pulses are

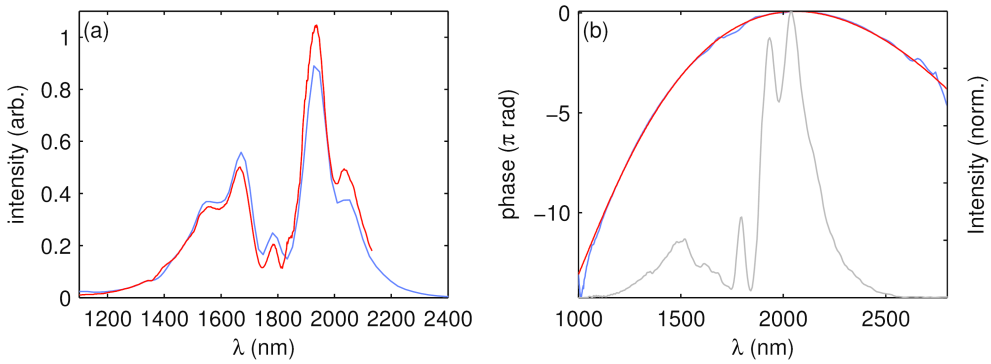

Fig. 3. (a) Spectrum reconstructed with SEA-F-SPIDER (blue) and fundamental measured on commercial InGaAs spectrometer (red), with maximum wavelength 2100 nm. (b) Measured (blue) and calculated (red) spectral phase introduced by 2.4 mm fused silica (left-hand y-axis); spectrum of pulse used for measurement (grey, right-hand y-axis).

faithful replicas of the test pulse.

Finally, to verify the accuracy of the reconstructed phase, Fig. 3(b) shows the difference between the reconstructed spectral phases with and without 2.4 mm fused silica in beam path (blue), and compares it with that predicted by linear propagation using a reference refractive index data. The excellent agreement is evidence of the accuracy of the technique and its calibration and also confirms that nonlinearities do not affect propagation in the bulk glass.

3. Results and discussion

3.1. Wavelength and pressure tuning

Figure 4(a) and (b) shows the measured spectral and temporal profiles at the center of the focus for an idler wavelength of 1800 nm. The other parameters are given in Table 1. The thickness of the fused silica wedges was adjusted to give the highest peak intensity. Compared to previous results [17] we increased the broadening slightly, producing a central peak of duration 1.3 optical cycles. In these terms, this is among the shortest pulses produced using HCF compression. As the pressure is adjusted there is a trade off between duration of the main peak and energy in the satellites, explored further below. The quality of the compression is reduced by uncorrected third-, fourth- and fifth-order spectral phase; numerical calculations show that successive correction of these orders by suitable chirped mirrors would decrease the effective duration (the ratio of energy to peak power) by ≈ 12% each. The reconstructions are precise; the shaded areas in Fig. 4 represent the extreme values over 10 consecutive measurements, with the corresponding standard deviation of the pulse duration being ≈ 0.1 fs.

Table 1. Parameters for tunable few-cycle pulse generation in Fig. 4.

Input						
Wavelength nm	Energy μJ	Duration FWHM fs	Spectral phase fs^2	Exit pressure bar	Output energy μJ	SiO_2 thickness mm
1800	1300	37	0	0.75	650	2.4
2060	1050	59	-670	1.6	500	1.7

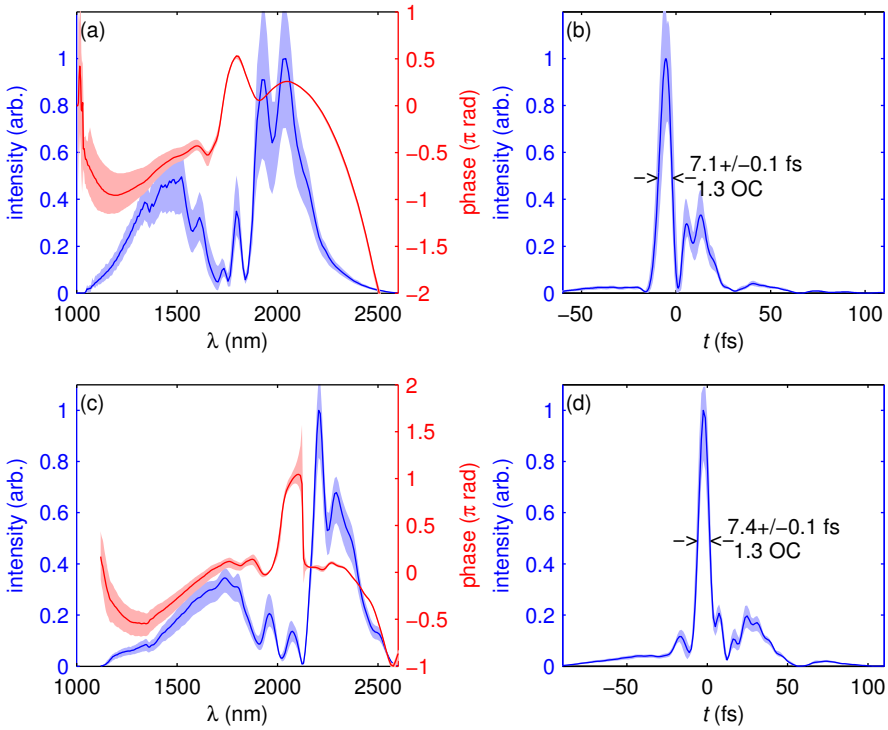

Fig. 4. Measured spectral and temporal profiles produced by compressing 1800 nm (a,b) and 2060 nm (c,d) pulses. (a) & (c): spectral intensity (blue, left y-axis), and phase (red, right y-axis). (b) & (d): temporal intensity with FWHM duration and equivalent number of optical cycles (OC) indicated. The shaded areas show the extremes (minimum and maximum) of 10 consecutive measurements; the lines show the average. Parameters are given in Table 1.

Figure 4(c) and (d) shows the temporal and spectral profiles after adjusting the TOPAS output wavelength to 2060 nm. Other parameters are given in Table 1. To achieve the same degree of broadening as the 1800 nm case, the required fiber pressure is approximately doubled. This is partially caused by the 20% reduction in TOPAS output power at 2060 nm compared to 1800 nm, but also because a significant negative chirp is introduced by the TOPAS optical components, which lowers the peak intensity and must be effectively "undone" by the positively chirped self-phase modulation (SPM). A consequence of this additional SPM is an additional oscillation in the middle of the spectrum. This is accompanied by sharp π phase jumps where the spectral intensity is nearly zero. The long wavelength tail of the spectrum is limited by absorption of water in the air, which sets in at 2550 nm.

Figure 5 shows the effect of adjusting the HCF exit pressure for the 2060 nm input wavelength case. Other parameters are given in Table 1. Increasing the pressure from 1.0 bar to 1.4 bar, the pulse duration drops below two optical cycles, with the pedestal remaining at the 10% level. A further increase to 1.8 bar results in a central peak of 1.2 OC, but due to significant pre- and postpulses it contains only 40% of the total energy.

3.2. Spatio-temporal reconstructions

Figure 6(a)–(c) shows the spatio-temporal reconstruction with input wavelength 2060 nm. The y-axis is scaled to match the fiber exit plane, so that the fiber walls are at $y = \pm 200\,\mu$m. The spatial uniformity and symmetry is good, and there is no significant tilt or distortion of the main

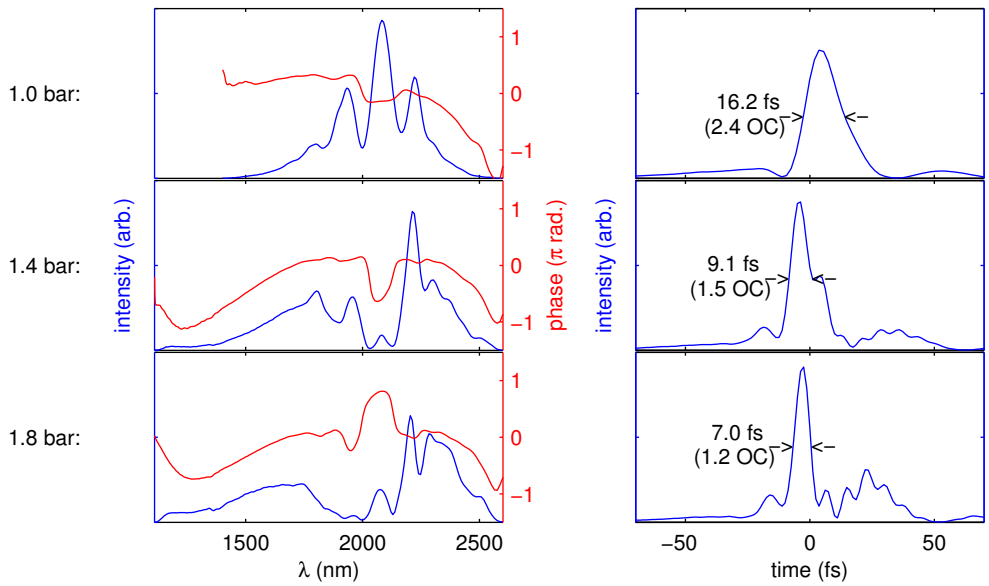

Fig. 5. Measured spectral and temporal profiles of pulses produced by broadening 2060 nm pulses for different HCF exit pressures (rows). Left column: spectral intensity (blue, left y-axis) and phase (red, right y-axis). Right column: temporal intensity, with FWHM duration and number of optical cycles indicated.

pulse front, although the weak trailing pulse at 50 fs is slightly tilted. (The vertical stripe in the phase at 1800 nm is an artefact of wrapping from $[-\pi, \pi]$.) This proves the effectiveness of the waveguiding in the fiber, even with our peak intensity of 80 TW/cm^2 which is just on the ionization threshold of argon. It also shows that no significant self-phase modulation is happening after the fiber exit (for example in the fused silica compression wedges) as this would cause spatially nonuniform spectral broadening.

To illustrate the reconstruction of nontrivial space-time couplings, we misaligned the HCF input beam by 6 mrad in the SEA-F-SPIDER measurement plane, keeping the position of the waist unchanged. This reduced the transmitted power by 30% and transferred a significant fraction of the launched energy to higher-order modes. The resulting spatio-temporal reconstruction is shown in Fig. 6(d)–(f). The spatio-spectral intensity distribution (Fig. 6d) is highly nonuniform and asymmetric, with significant variation of the bandwidth across the beam. Correspondingly, the temporal intensity profile varies significantly in duration, arrival time and shape of pre- and postpulses across the beam. Although our misalignment was deliberate, coupling into higher-order modes can easily occur through accidental fiber bending or a poor input beam quality, and this example shows how the SEA-F-SPIDER is sensitive to these problems and is thus a useful diagnostic in these cases.

While the input misalignment in the previous example causes coupling to several higher-order modes, a reduction of the input focus size from the optimum [39] transfers energy predominantly to the HE_{12} mode. With only one higher-order mode present, interference becomes clear in the output spatio-spectral distribution. Figure 7(a) shows a measurement in which the input focus FWHM is 135 µm, 10% smaller than that required for optimal coupling to the fundamental mode. The spectral intensity is spatially uniform except from 1700–1900 nm, where structure is present. To interpret this structure we used a propagation model [40] featuring coupled HE_{1m} cylindrically symmetric modes, mode-dependent dispersion and loss curves, and the Kerr

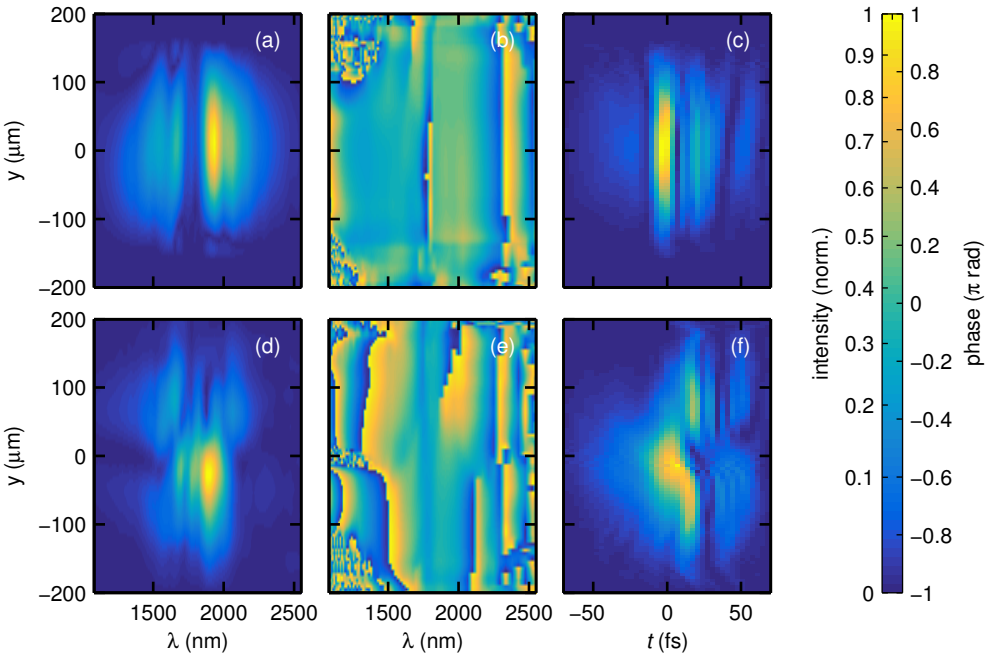

Fig. 6. Spatio-temporal reconstructions with input wavelength 2060 nm and HCF exit pressure 1.4 bar; (a) & (d) show spectral intensity, (b) & (e) show spectral phase, and (c) & (f) show temporal intensity. In panels (a)–(c), the HCF input coupling is optimized, whereas in panels (d)–(f), the input beam is misaligned by 6 mrad. Note that the intensity color scale is nonlinear to improve the visibility of low amplitude features.

nonlinearity with self-steepening. The launched modal amplitudes are calculated by overlap integrals with a Gaussian beam matched to the experimental focal size. Here, we present the calculated spatio-spectral intensity distribution in Fig. 7(b). The interferometric structure is qualitatively reproduced, and can be interpreted using the transverse mode profiles shown in Fig. 7(c) along with the simulated spectral densities of the fundamental and HE_{12} mode at the fiber output, shown in Fig. 7(d). Compared to the input spectrum (red), the output HE_{12} spectrum (green) is blue-shifted and spectrally broadened by cross phase modulation. At 1750 nm the fundamental mode spectrum (blue) has a null and so the spatial profile is dominated by the narrower distribution of the HE_{12} mode. On either side of 1750 nm the modes are of comparable amplitude but out of phase, resulting in an annular distribution. We considered other possible explanations for the structure from 1700-1900 nm, including additional self-phase modulation in the fused silica wedges or the exit chamber of the fiber where propagation is unguided, but could not reproduce the observation. The ability to diagnose such subtle mode coupling effects may be useful in situations where multiple waveguide modes play a crucial role, such as quasi-phase matching for HHG [41] or supercontinuum generation in photonic crystal fibers [42].

3.3. Discussion

As with all SEA-SPIDER configurations, the focused beam is sampled by the input slit of the imaging spectrometer, so the reconstructions have only one spatial dimension; we reconstruct $E(t, y; x_0)$ at a central slice $x = x_0$ of the focus. The reconstruction could be made three dimensional in a limited sense using techniques of hyperspectral imaging, the simplest being the "pushbroom" method of scanning the upconverted beams perpendicularly to the slit, and

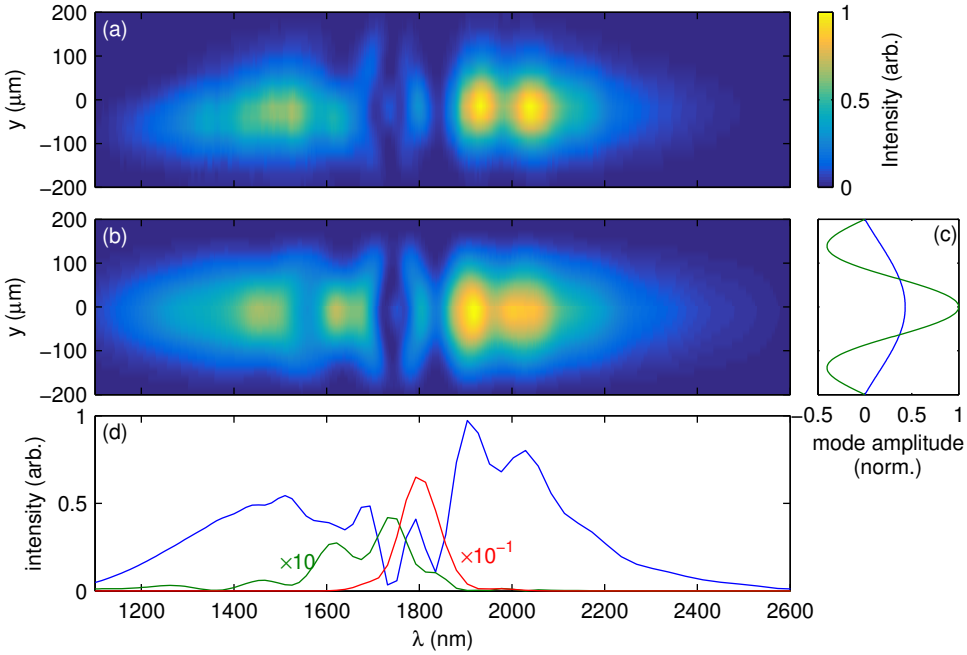

Fig. 7. Spatio-spectral distribution with a smaller-than optical input focus FWHM of 135 µm and input wavelength 1800 nm; other parameters in Table 1, (a) measured (b) simulated. (c) Amplitude profiles of the fundamental (blue) and HE_{12} (green) modes. (d) Simulated spectral density of input pulse (red), output fundamental mode (blue), and output HE_{12} mode (green).

concatenating the resulting two-dimensional reconstruction slices. However, unless great care is taken with calibration, the relative group delay between slices would not be returned. Another approach would be to rotate the test pulse going into the device so as to obtain a series of slices at different angles, with the pulse fronts of each slice referenced to a common point, the rotation axis. This would allow determination of the pulse front in both spatial dimensions.

Besides hollow fiber compressors, the technique presented here should be useful for studying other few-cycle pulse sources with potential space-time coupling, such as filamentation [13] or OPCPA [12]. It will also be useful to observe pulses after nonlinear propagation in a target medium. For example, the spatio-temporal profile of a pulse after HHG will give insight into the reshaping caused by the plasma blue-shift and defocusing, which strongly affects high-order harmonic generation [43]. The use of a separate, shorter wavelength for the ancillae to bring the upconverted signals into the visible region is also attractive for the mid-infrared, enabling high sensitivity and high resolution with silicon detector arrays.

4. Conclusion

In conclusion, we presented the first spatio-temporal reconstructions of few-cycle pulses at 1.8–2.1 µm. The pulses had a duration of 1.3 optical cycles, among the shortest pulses produced using HCF compression. With a well aligned HCF, we obtained a high degree of spatial uniformity with no significant pulse front distortions, and demonstrated adjustment of the pulse duration and center wavelength. We also explored the effect of HCF misalignment and mismatch of the input mode area, and verified the ability of SEA-F-SPIDER to retrieve pulse front tilt caused by angular dispersion in ≈ 2 cycle pulses, the shortest ever used in such a measurement. The

measurement device is extensible to longer wavelengths and should be useful for the optimization of the next generation of mid-infrared sources for strong-field physics.

Funding

This research was supported in part by EPSRC program grant EP/I032517/1, ERC ASTEX project 290467, Marie Curie ITN EC317232, and the NSERC PGS program. DRA acknowledges support of an Imperial College Junior Research Fellowship.